Operando measurement of lattice strain in internal combustion engine components by neutron diffraction

Martin L. Wissink[a,1], Yan Chen[b], Matthew J. Frost[b], Scott J. Curran[a], Orlando Rios[c,d], Zachary C. Sims[c,e], David Weiss[f], Eric T. Stromme[c,g], and Ke An[b]

[a]Energy Science and Technology Directorate, Oak Ridge National Laboratory, Oak Ridge, TN 37831; [b]Neutron Sciences Directorate, Oak Ridge National Laboratory, Oak Ridge, TN 37831; [c]Physical Sciences Directorate, Oak Ridge National Laboratory, Oak Ridge, TN 37831; [d]Department of Materials Science and Engineering, The University of Tennessee, Knoxville, TN 37996; [e]The Bredesen Center for Interdisciplinary Research and Graduate Education, The University of Tennessee, Knoxville, TN 37996; [f]Eck Industries, Inc., Manitowoc, WI 54220; and [g]US Navy, Washington, DC 20350

Edited by Alexis T. Bell, University of California, Berkeley, CA, and approved November 2, 2020 (received for review June 22, 2020)

Engineering neutron diffraction can nondestructively and noninvasively probe stress, strain, temperature, and phase evolutions deep within bulk materials. In this work, we demonstrate operando lattice strain measurement of internal combustion engine components by neutron diffraction. A modified commercial generator engine was mounted in the VULCAN diffractometer at the Spallation Neutron Source, and the lattice strains in both the cylinder block and head were measured under static nonfiring conditions as well as steady state and cyclic transient operation. The dynamic temporal response of the lattice strain change during transient operation was resolved in two locations by asynchronous stroboscopic neutron diffraction. We demonstrated that operando neutron measurements can allow for understanding of how materials behave throughout operational engineering devices. This study opens a pathway for the industrial and academic communities to better understand the complexities of material behavior during the operation of internal combustion engines and other real-scale devices and systems and to leverage techniques developed here for future investigations of numerous new platforms and alloys.

neutron diffraction | operando | in situ | internal combustion engine | time-resolved

The internal combustion engine (ICE) converts the chemical energy stored in fuel into mechanical energy by the direct force on engine components applied from the expansion of high-temperature and high-pressure gases produced by combustion (1). This process presents many materials challenges as work extraction is performed in a highly dynamic, reactive, and corrosive environment producing extreme absolutes and temporospatial gradients of temperature and pressure. In a reciprocating engine, both the stationary components (e.g., cylinder head, liner, and manifolds) and the moving components (e.g., pistons and valves) undergo complex thermomechanical cycles at frequencies ranging from less than 1,000 rev/min at idle to nearly 20,000 rev/min in racing applications. Both spark-ignited (gasoline) and compression-ignited (diesel) engines undergo rapid release of chemical energy, producing extremely transient load states and thermal gradients inside the combustion chamber. It is common for engines to operate at peak gas temperatures exceeding 2,200 °C and peak pressures ranging from 0.5 to 2.5 MPa with pressure rise rates of 10 to 50 MPa/ms (2), and during abnormal combustion events such as preignition and detonation, pressure rise rates can exceed 100 MPa/ms (3). Heat fluxes through the various surfaces in the combustion chamber can vary dramatically at different locations due to inhomogeneity of the combustion gases (4) and may locally exceed 10 MW/m^2 for periods of several ms when burning fuel jets impinge upon surfaces (5). Development and adoption of new materials with improved mechanical and thermal integrity can increase reliability and enable higher efficiency while also making space for elevated operational temperatures and the use of forced air induction technologies, further increasing efficiency gains. Additionally, if new materials are adopted which possess higher specific strength, there is potential to improve transient load response times and to improve vehicle fuel economy through lightweighting. Laboratory-scale investigations of engineering materials by physical simulation are often conducted in attempt to meet the requirements of rigorous operation. Understanding the dynamic behavior such as temperature, stress, and strain during operation is valuable for new materials development and for engineers seeking to design improvements to efficiency, durability, and safety. However, due to the lack of a nondestructive evaluation tool that can emulate the real operating conditions inside an ICE, true understanding of operando dynamic thermomechanical behaviors and responses of the engine components is limited.

Recent advances in neutron sources and neutron instrumentation allow probing of materials behavior in complex in situ sample environments in both reduced length and time scales (6–8). The Spallation Neutron Source (SNS) at Oak Ridge National Laboratory (ORNL) is the world's most intense time-of-flight (TOF) neutron facility, and the high neutron flux provides opportunities to perform neutron diffraction measurements with high resolution over a range of temporal and spatial scales in engineering applications (6, 7, 9). Neutron diffraction is often used for measuring lattice strains (10, 11) due to temperature

Significance

Internal combustion engine components experience extreme thermomechanical cycling during operation, and the continuing need to improve engine efficiency while maintaining or improving reliability drives the development of lightweight materials with improved thermal and mechanical integrity. Understanding the behavior of new materials in dynamic operation requires operando characterization tools, but conventional in situ measurements of material behavior during real engine operation are very limited, and no practical means exist to replicate such extreme dynamics for ex situ study. In this work, we demonstrate that the penetrating power of neutrons can provide noninvasive measurement of lattice strains inside components of a firing engine, enabling the operando study of complex load states and thermal gradients throughout the solid materials.

Author contributions: Y.C., M.J.F., O.R., Z.C.S., D.W., E.T.S., and K.A. designed research; M.L.W., Y.C., M.J.F., S.J.C., O.R., Z.C.S., E.T.S., and K.A. performed research; M.L.W., Y.C., and K.A. analyzed data; and M.L.W., Y.C., S.J.C., O.R., Z.C.S., and K.A. wrote the paper.

The authors declare no competing interest.

This article is a PNAS Direct Submission.

[1]To whom correspondence may be addressed. Email: wissinkml@ornl.gov.

or stress, microstructure texture and its evolution, and phase fractions deep inside engineering components which even high-energy X-rays cannot penetrate, making neutrons unique for studying the behavior of materials in large structures (12). The VULCAN engineering materials diffractometer (13, 14) at the SNS is designed for deformation, phase transformation, residual stress, and texture studies in engineering materials which are typically under laboratory-scale physical simulation with applied load and temperatures. The incident slits and collimation in front of the ±90° diffraction detector banks (14) allow probing a small voxel or gauge volume inside a structure or device even under operando conditions. The time-event neutron data acquisition system records the full pattern of diffracted neutrons with timestamps and enables straightforward time-resolved measurement (7, 15). These advantages of TOF neutron engineering diffraction open a great opportunity to investigate real-time material dynamic response under realistic operating conditions. Taking advantage of these unique capabilities at VULCAN, we demonstrate measurement of lattice spacing changes due to temperature and stress within the cylinder head of an ICE during transient operation. An asynchronous pump-probe or stroboscopic neutron measurement (7, 16–18) was employed to resolve the rapid time-dependent behaviors. This work shows the future potential of measuring fast operando dynamics of targeted, specific engine components using the deep penetration power of high-flux neutrons at the SNS.

Experimental Setup

Operando Engine Experimental Platform. To demonstrate the feasibility of safely operating a running engine as an operando experimental platform at VULCAN, a commercially available electric generator powered by a carbureted small-bore single-cylinder ICE was modified and commissioned in an engine test cell at the National Transportation Research Center (NTRC). The NTRC is a DOE user facility located at ORNL and is equipped for research on innovative ICE technologies and control systems. The specifications of the modified ICE are given in Table 1. A diagram illustrating the configuration of the engine and relative location of the gauge volumes is shown in Fig. 1*A*.

There were several unique constraints for this experiment related to the limited physical sample space within the diffractometer, lack of specialized engine test facilities such as a dynamometer within the diffractometer, and the fact that neutrons are strongly attenuated by ^{1}H due to its large incoherent scattering cross section. This experimental platform was chosen and developed with the following safety and data acquisition considerations: 1) the experimental setup allowed for self-contained practical operation of a running engine, 2) the compact overall size fit within space constraints at VULCAN, 3) the integrated generator removed the need for a standalone dynamometer to accept load from the engine, 4) the engine was air-cooled and thus did not face concerns with strong neutron attenuation or scattering background by hydrogenous coolant, 5) the pushrod two-valve layout minimized the amount of steel components in the cylinder head that could attenuate the scattered neutrons from the gauge volume(s), 6) the relatively simple design of the lubrication system did not feature any oil passages along the top or front of the engine that could attenuate the incident or scattered neutrons, and 7) the electric starter allowed the engine to be started remotely.

Table 1. Generator and engine specifications

Property	Value
Generator	
Model	Honda EU3000is
Rated AC output	120 V, 2.8 kW (23.3 A)
Rated DC output	12 V, 144 W (12 A)
Engine	
Model	Honda GX200
Swept volume	196 cc
Bore × stroke	68 × 54 mm
Compression ratio	8.5
Net power	4.1 kW @ 3,600 rpm
Net torque	12.4 Nm @ 2,500 rpm

Beyond the relevant VULCAN-specific experimental considerations addressed by using an air-cooled engine, the geometric complexity presented by the cooling fins and internal geometry of the part made it a good test bed for the castability of an aluminum cerium (AlCe) alloy codeveloped by ORNL and Eck Industries. The Honda GX200 cylinder head geometry was measured by X-ray computed tomography and imported to a CAD model through scanning software. Once imported, the molds for use with sand casting were printed using a binder jet additive manufacturing system (19). This method eliminated the long lead time for traditional tooling and lowered the cost for a small-batch prototype run, and the resulting AlCe cylinder head is shown alongside the original cylinder head in Fig. 2. The benefits of this technology could be used by future experimenters to quickly test new materials or how system geometry affects cooling and internal strain during operation. The AlCe alloy from which the head was produced was developed through a Critical Materials Institute project and is being positioned for high-temperature applications where aluminum alloys have long struggled to find applications. The alloy uses as a primary addition the element cerium and has the composition of Al-12wt% Ce-0.4wt%Mg. This composition was selected as it falls near the Al-Ce eutectic creating a castable material, and prior neutron research conducted on this alloy shows minor additions of Mg to have large positive impacts on load sharing capability of the majority $Al_{11}Ce_3$ intermetallic (20). The high thermal stability of strengthening aluminum-cerium intermetallics which are formed during solidification at traditional casting rates, as opposed to being precipitated during costly, long heat treatments, makes the material a good candidate for next-generation ICEs. Thermal stability of the alloys results from the near-zero solubility and accompanying low diffusivity of Ce in the aluminum matrix meaning the strengthening cerium-rich intermetallic phases are locked in at solidification and only see minor, nondetrimental morphological changes during long exposure to elevated temperatures (20).

The engine/generator platform was prepared for use in the neutron diffractometer by first removing the mounting frame, external casing, and all extraneous covers and plastic components in order to minimize neutron attenuation. The steel fuel tank was removed and replaced by a remote fuel tank connected by a flexible hose. The steel muffler was removed and replaced by a section of exhaust pipe that was fitted with a type-K thermocouple to allow measurement of the exhaust temperature. In order to obtain meaningful neutron diffraction results during engine operation, it is essential that the gauge volume being targeted remains constant during each measurement. To that end, the stripped-down assembly was rigidly mounted to an aluminum breadboard in order to minimize vibrational displacement of the engine during operation, and the final instrumented assembly is shown mounted at VULCAN in Fig. 1*B*. Note that the term "displacement" is used here to refer to the amplitude of vibrational movement within the engine structure and not the swept volume of the engine.

Offline testing was performed at the NTRC to assure safe and reliable operation of the modified engine before neutron diffraction experiments were performed at VULCAN. Vibrational displacement was measured by a three-axis accelerometer (PCB Piezotronics Model 356B21) mounted to the crank case, as well as a laser triangulation sensor (Microtrak 3) aimed at the location of interest on the cylinder head. The engine was operated at

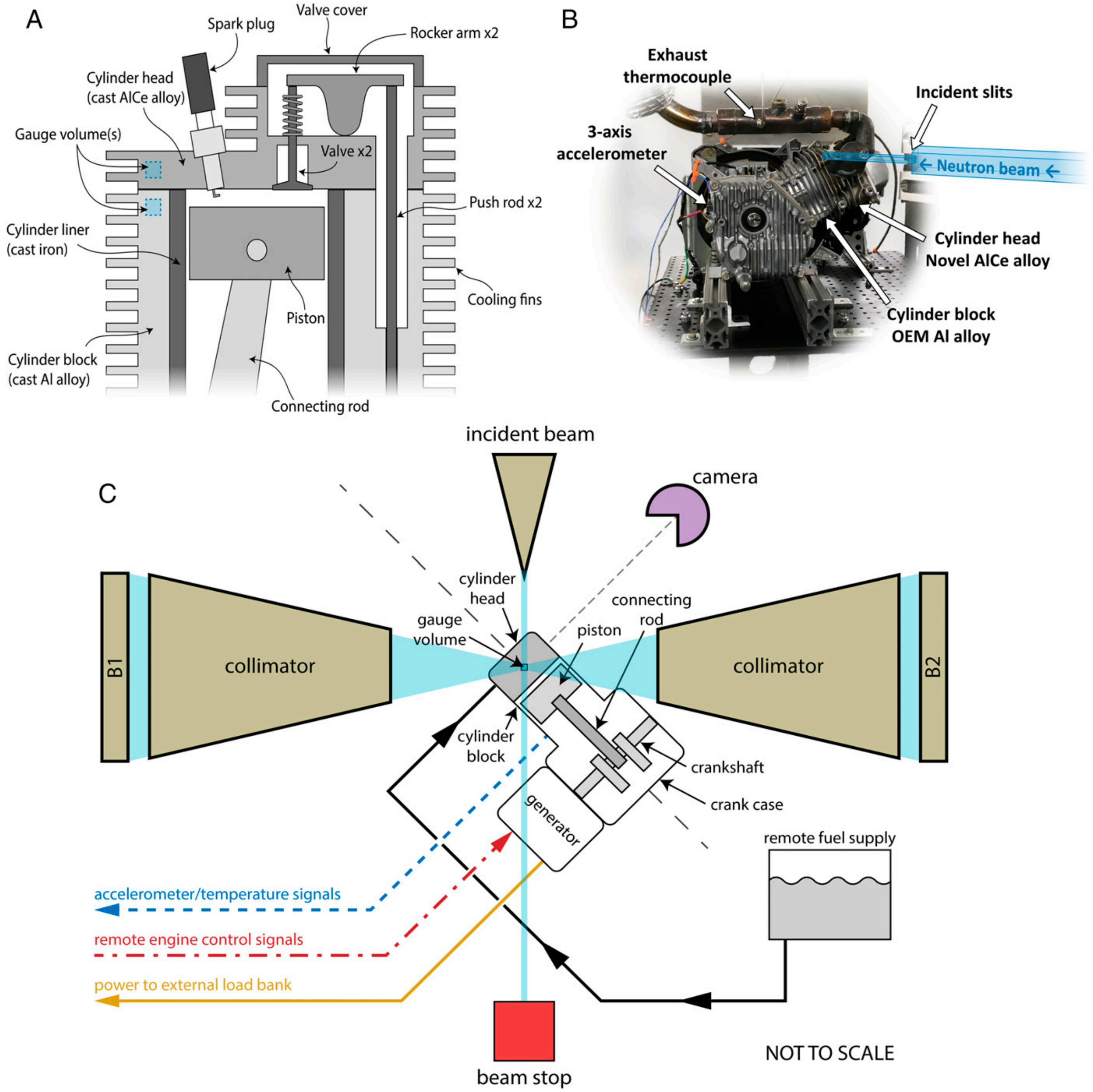

Fig. 1. Experimental details. (*A*) Cross-sectional diagram of the air-cooled, single-cylinder engine with representative locations of gauge volumes highlighted in both the head and cylinder block. (*B*) Picture of the modified engine installed at the VULCAN beamline with instrumentation. (*C*) Diagram of experimental configuration (view from above), showing engine installed along the 45° plane bisecting incident beam and detectors (B1 and B2) with gauge volume located in the cylinder head. Camera lies along orthogonal 45° plane with view shown in Fig. 4.

three load conditions by placing an electrical load on the generator with a programmable load bank. These conditions were 0 (engine idle), 1,530, and 2,586 W, which correspond to 0, 55, and 92% of the rated generator load, respectively. The generator also features an Eco-Throttle setting which reduces engine speed at idle to reduce fuel consumption and noise, and this mode was tested as well. The rms values of vibrational displacement (rms displacement) measured by the accelerometer and laser are shown in Fig. 3. The lowest rms displacement levels were seen at idle with the Eco-Throttle enabled, whereas the rms displacement was relatively insensitive to load with the setting disabled. The trendwise agreement between all measurements was good, and the overall magnitude of the laser and the accelerometer z axis were in close agreement. All measured values of rms displacement were below 0.5 mm, which represents a 10% threshold for the 5-mm gauge length used in this study.

After the commissioning was successfully performed at the NTRC ensuring safe operation and acceptable vibrational displacement while running in the modified configuration, the engine and support systems were installed at VULCAN. A diagram

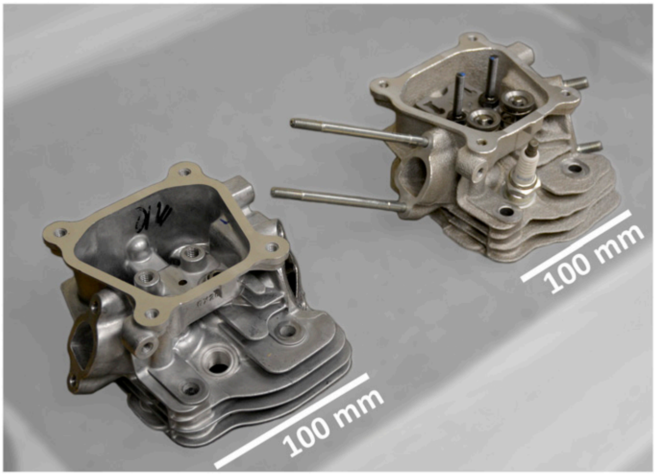

Fig. 2. OEM production cast cylinder head (*Left*) pictured next to AlCe cylinder head (*Right*) produced from 3D-printed molds. Cylinder head hardware including mounting studs, valves, and spark plug was transferred from the OEM head to the AlCe head.

in Fig. 1*C* shows the layout of the operando experiment. The engine and generator assembly were mounted atop the translation/rotation stage at the intersection of the incident beam and collimators (14). The remote fuel supply was located near the engine but out of the direct beam path and at a higher elevation such that the fuel could gravity feed to the carburetor without the need for a fuel pump. Signals from the accelerometer and exhaust temperature thermocouple were routed to the data acquisition system for live monitoring of the engine status. The engine was controlled by a remote starter and cutoff switch located in the VULCAN control room. The power output from the generator was metered by a programmable load bank located outside of the VULCAN experiment enclosure and adjacent to the control room. All wiring and hoses connected to the engine and generator were positioned out of the beam paths and anchored with strain relief to allow for translation and rotation of the engine assembly during operation. The exhaust from the engine was routed into the facility's exhaust extraction system with a flexible duct.

External Infrared Temperature Measurement. In addition to the thermocouple measurement of the exhaust gases, an infrared (IR) camera (FLIR T450sc) recording at 30 frames per second was used to monitor the temperatures of the external surfaces. The IR camera point of view was similar to that of the sample positioning camera illustrated in Fig. 1*C*. Emissivity was calibrated by use of a surface-mount thermocouple placed on the cylinder head; therefore, the IR temperature values and images such as Fig. 4 are quantitative only for the AlCe cylinder head and are qualitative elsewhere.

Neutron Diffraction Measurement of Static and Dynamic Lattice Strains. The layout of the operando neutron diffraction measurement is illustrated in Fig. 1*C*. The incident beam at the SNS is pulsed and operates at 60 Hz. The neutron energy and wavelength are resolved and quantified by the recorded TOF of neutrons with every pulse emitting time and time traveled over the fixed flight path of the instrument. A 30-Hz chopper setting was used to allow a broad measurement range of lattice interplanar spacing (d-spacing) from 0.5 to 2.5 Å. The incident beam was collimated to 5×5 mm^2 by the motorized incident slits ahead of the sample. Although the incident beam is scattered all along the length of its path through the sample, radial receiving collimators affixed to the two opposite detector banks B1 and B2 located perpendicular to the incident beam (±90°) restrict the angular range from which scattered neutrons may reach the detectors, resulting in a $5 \times 5 \times 5$ mm^3 gauge volume as illustrated in Fig. 1*C*. Each detector bank measures lattice spacing changes along the bisectors of the angles between the incident beam and the diffracted beam (±45°). Due to the pulsed TOF beam configuration, the individual location-specific lattice d-spacings within the gauge volume can be measured at once without the need to rotate the sample or detectors. More details about the engineering diffraction setup can be found in previous work (14). Because the positions of the incident beam and detector banks are fixed, the location of the gauge volume within the engine was manipulated by repositioning the entire engine setup using the instrument sample stage.

Results and Discussion

Spatial Mapping of Lattice Strain Distribution. In order to demonstrate the feasibility of spatially resolved operando neutron diffraction in an ICE, diffraction patterns were collected over a two-dimensional (2D) grid spanning 55 mm × 75 mm at 5-mm intervals (11 × 15 measurement locations), as illustrated in Fig. 4. This grid was located below the external surface of the engine in a region straddling the interface between the cylinder block, which is composed of the cast Al alloy supplied by the original equipment manufacturer (OEM), and the cylinder head, which is composed of the cast AlCe alloy. Because both alloys are Al-based, they both contain a face-centered cubic (FCC) matrix phase with Bragg peaks from the (222) and (311) planes. In general, the d-spacing of a given set of lattice planes (hkl) can be related to the lattice parameter a, which defines the size of the FCC unit cell, by

$$d_{hkl} = \frac{a}{\sqrt{h^2 + k^2 + l^2}}. \qquad [1]$$

The lattice strain can then be defined at a given location (x, y, z) by comparison of the measured value of $d_{hkl}(x, y, z)$ to a reference value $d^0_{hkl}(x, y, z)$:

$$\epsilon_{hkl}(x,\ y,\ z) = \frac{d_{hkl}(x,\ y,\ z) - d^0_{hkl}(x,\ y,\ z)}{d^0_{hkl}(x,\ y,\ z)}. \qquad [2]$$

When mapping the residual strain within a sample, a single value of d^0_{hkl} obtained from a well-characterized stress-free reference is

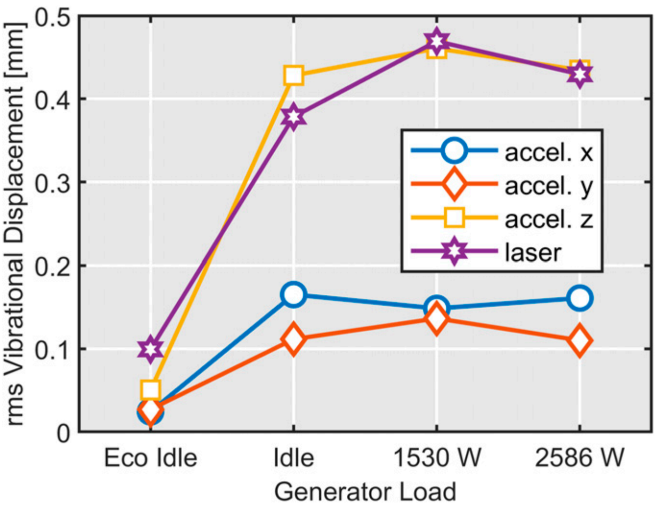

Fig. 3. Vibrational displacement of external engine structure at four operating conditions as measured by three-axis accelerometer and laser displacement sensor. All measurements show rms value <0.5 mm or less than 10% of the gauge volume dimension.

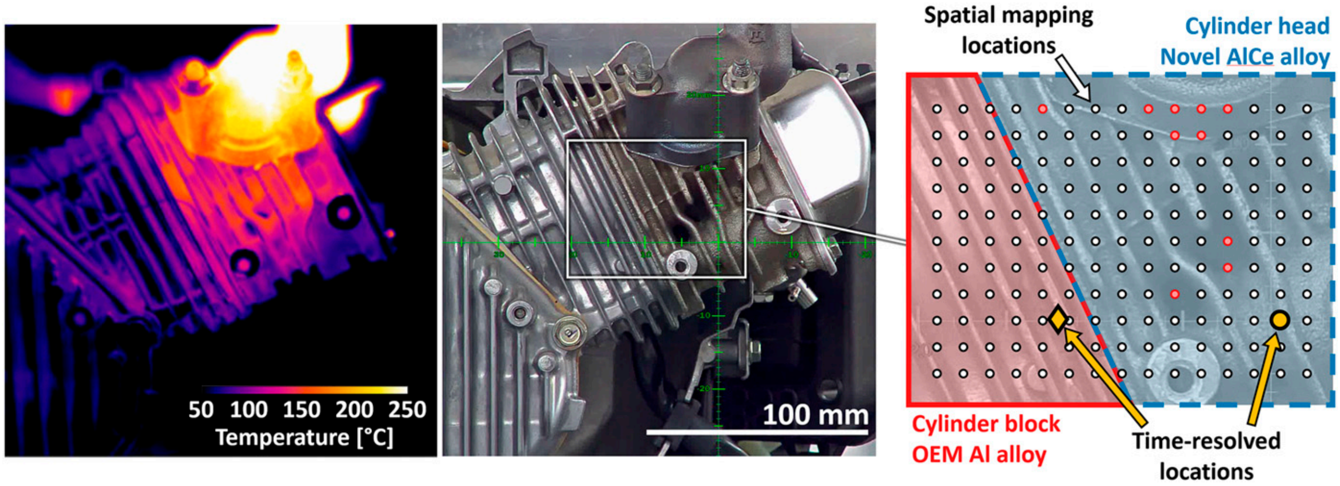

Fig. 4. (*Left*) Infrared temperature image of the engine 1 min after startup. (*Middle*) Photograph of the engine from the sample alignment camera. (*Right*) The 11 × 15 spatial mapping locations (white-filled circles) and the selected points in the cylinder block (yellow-filled diamond) and cylinder head (yellow-filled circle) for time-resolved strain measurements. Locations with red-shaded circles had poor fitting statistics in one or more of the spatial mappings, primarily due to the open internal region in the exhaust port (top cluster) and recessed areas of the casting which may have had partial burial of the gauge volume (middle cluster).

often used. However, for dynamic strain measurements in large engineering components, it is not appropriate to use a single value of d^0_{hkl} due to spatial variations in composition. The residual stresses from casting, manufacturing, assembly, and previous operation make it difficult to nondestructively measure the true stress-free d-spacings throughout the system. In many cases, knowledge of what value to use for d^0_{hkl} may also be unavailable due to unknown provenance, composition, and history of the sample in question. Further, the complexity of the sample geometry may inevitably introduce artifacts due to the neutron gauge volume being only partially filled by the material at some measurement locations (partial burial) (10), such as when near the surface.

Here we chose the reference lattice values $d^0_{311}(y, z)$ based on a spatially resolved mapping at the initial condition of the engine, which allows for calculation of relative strain evolution during engine operation. This reference mapping was conducted with the engine off and under ambient room temperature (~25 °C) conditions over the previously described 2D grid, and each location was measured for roughly 1 min. The FCC (311) Bragg peak was chosen as the representative to calculate the lattice strains because it is least affected by intergranular strains resulting from material anisotropy (10) and other localized information such as casting texture. The (311) peak d-spacings were determined via single peak fitting using Data Reduction and Interactive Visualization software for Event Mode Neutron Diffraction (VDRIVE) (21). The resulting reference mapping is visualized in Fig. 5*A* as a pseudocolor plot. The interface between the cylinder head and block is clearly visible, with the head tending to have higher measured d_{311} values due to the different alloy composition. There is also variation of d_{311} within each component, which may be a result of assembly stresses and spatial variation in casting cooling rate and alloy solid solutions. Fig. 5*A* shows that location-specific $d^0_{311}(y, z)$ is essential for accurate strain response calculation under engine operation.

Note that not all measurement locations were used in the production of the reference mapping visualization—several were excluded due to poor peak-fitting statistics. These locations are also annotated in Fig. 4 and fall into two major clusters. The cluster at the top of the map coincides with the exhaust port, which is an open area (as seen in Fig. 2) where little or no material occupies the gauge volume. The cluster near the middle of the map coincides with recessed areas of the casting which also may have had partial burial of the gauge volume. Two example diffraction patterns from the reference mapping are shown in Fig. 5*B*. One is from a location with good peak fitting statistics which has clearly discernable (222) and (311) peaks. The other pattern is from a location in the exhaust port, has no discernable peaks relative to background, and was excluded from the mapping visualization.

Following the reference mapping, the lattice expansion due to temperature rise under steady-state engine operation at a generator load of 2 kW was mapped by measuring for roughly 2 min per location. While certain components in engines, in particular the exhaust valves (22), any areas impinged upon by fuel sprays (5, 23, 24), and other internal surfaces of the combustion chamber such as the liner and piston rings (25), are subject to rapid temperature oscillations during the combustion cycle, these generally occur over a time scale on the order of ms, and the penetration of the thermal wave into the engine structure is on the order of hundreds of μm due to the high thermal capacitance of metals. For our measurements taken near the outer surface of the engine structure, the temperature within the gauge volume will be effectively constant provided that the engine is at a constant power output and has reached a steady-state thermal condition.

The operando $d_{311}(y, z)$ map is shown in Fig. 5*C* and was prepared in a similar manner as the reference map in Fig. 5*A*. The operando map was measured near the end of the allocated beamtime, and an exhaust leak caused a premature end to the experiment and an incomplete map due to limited remaining beamtime available for troubleshooting and repair. However, the proof of principle is shown by this measured dataset. The two maps have a broadly similar appearance, but note that the color scale for the operando map in Fig. 5*C* has been shifted to larger d-spacing values due thermal expansion of the materials. Using these two maps, the spatially resolved operando lattice strain $\epsilon_{311}(y, z)$ was calculated using Eq. **2** and is shown in Fig. 5*D*. Because values are required from both input maps in order to calculate strain, the excluded points in the $\epsilon_{311}(y, z)$ map are the union of the exclusions in the input maps. The measured lattice strain ranged from a low of 2,365 ± 112 microstrain (με) in the cylinder block to a high of 4,096 ± 86 με in the cylinder head and increased monotonically toward the upper right corner of the

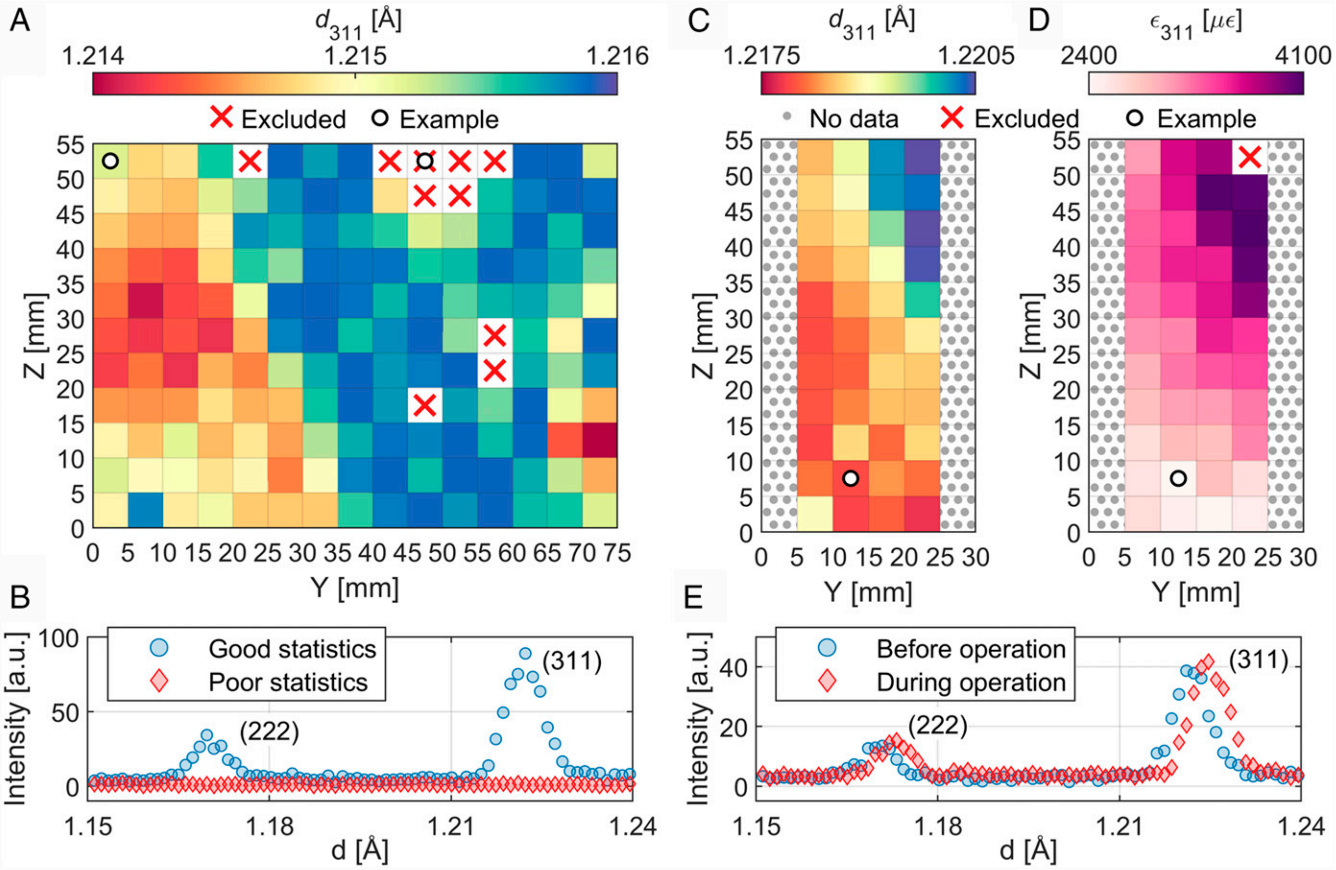

Fig. 5. (*A*) Spatial mapping of (311) Bragg peak location (d_{311}) in the engine at room temperature in a static reference condition as shown by pseudocolor map. Locations marked by a red X were excluded from visualization due to poor peak fitting statistics, and examples of good- and poor-quality spectra are highlighted by white-filled filled circles and shown in *B*. Interface between the cylinder head and block is clearly visible in the d_{311} map and corresponds to the regions highlighted in Fig. 4. (*B*) Location with good peak fit statistics has clearly visible (222) and (311) peaks, while the location with poor statistics has no discernable peaks relative to background. (*C*) Spatial mapping of d_{311} at hot steady-state engine operation—only partially completed due to time limitations. Note that scaling is different from that in *A*. (*D*) Lattice strain map (ϵ_{311}) as calculated by comparing d_{311} during steady-state engine operation (*C*) and the static reference condition (*A*). Excluded points in *D* are the union of exclusions from *A* and *C*. Strain increases monotonically toward the upper right corner of the figure, which is near the hot exhaust port (Fig. 4). (*E*) Example spectra from a single location used for strain calculation have clearly visible shifts in the locations of both (222) and (311) peaks due to thermally induced strain.

map, which is nearest to the hot exhaust port as seen in Fig. 4. Using the measured coefficient of thermal expansion (CTE) of 23.5×10^{-6} °C^{-1} for the AlCe cylinder head alloy and assuming that the strain is entirely due to thermal expansion results in an estimated temperature increase of 174.3 ± 5.2 °C, or an absolute temperature of ~200 °C at the highest strain location of the map. Typical alloys used for cast Al cylinder blocks have CTE in the range of 21 to 24×10^{-6} °C^{-1} (26). Using the CTE of 21.8×10^{-6} °C^{-1} for A380, which is the most common Al die casting alloy, results in an estimated temperature increase of 108.5 ± 5.7 °C, or an absolute temperature of ~133 °C at the lowest strain location of the map. Good qualitative agreement is seen between the subsurface lattice strain (and inferred temperature) in Fig. 5*D* and the IR surface temperature measurements shown in Fig. 4.

After the engine was stopped and fully cooled down, the same region was remapped by the same measurement grid, and the resulting $d_{311}(y, z)$ map is shown in Fig. 6*A*. Using the reference map in Fig. 5*A* as $d^0_{311}(y, z)$, the lattice strain $\epsilon_{311}(y, z)$ was calculated for each location using Eq. **2**. The resulting microstrain map in Fig. 6*B* is rather flat, with most locations within ±100 με, which is approaching the resolution limit of the diffraction technique. Example before-and-after diffraction patterns from a location in the cylinder head are shown in Fig. 6*C* and demonstrate that the peaks have returned to nearly identical positions. This before-and-after mapping demonstrates that the cast AlCe alloy engine head is unlikely to undergo morphological or phase changes during engine operation (20). It also confirms that our approach of measuring individual location-specific references is effective to eliminate the contribution of the variations of the reference lattice d-spacing and enable quantification of strains that are comparable throughout the measured engine region.

Time-Resolved Lattice Strain Response during Engine Operation. To study the dynamic lattice strain response during engine operation, one location within the cylinder block and one location within the AlCe cylinder head were selected, as illustrated in Fig. 4, Right. The engine was manually operated in three-part load transient cycles consisting of engine startup and idle (0 kW generator load) for 2 min, a step change to 2 kW generator load (~50% of rated power) held for 5 min, and engine shutdown with a 6-min cooldown period. Because the neutron flux is insufficient to capture real-time diffraction patterns at these time scales, continuous asynchronous stroboscopic measurement of multiple load transient cycles was employed to resolve the time-varying response of the system. The transient load cycle was repeated 21 times while time-event neutron diffraction data and exhaust

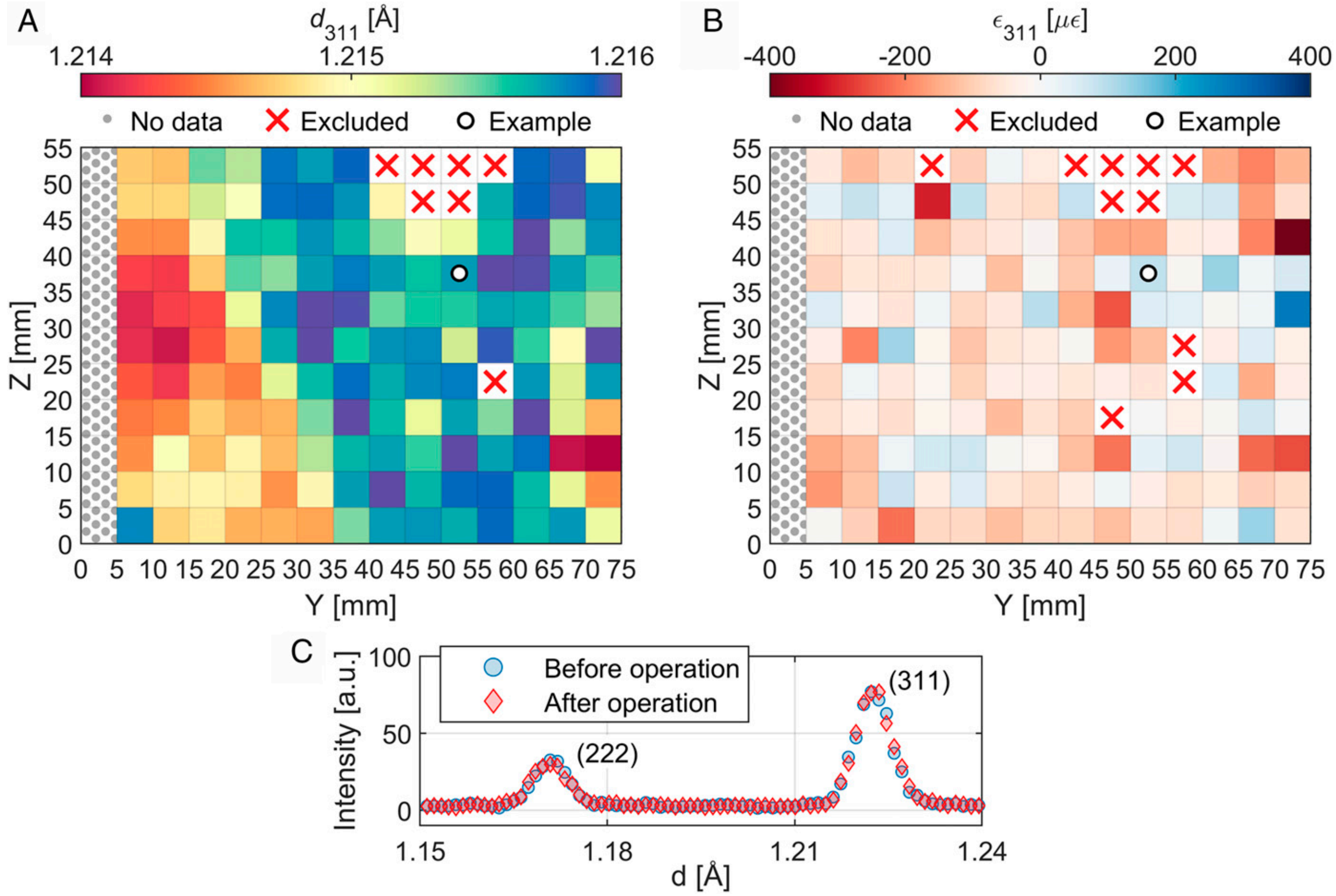

Fig. 6. (*A*) Spatial mapping of d_{311} after engine was shut down and allowed to cool to room temperature, with the same scaling as Fig. 5*A* and overall similar appearance. (*B*) Lattice strain map after cooldown indicates that most regions have residual strain <100 $\mu\epsilon$. Excluded points are the union of exclusions from Figs. 5*A* and 6*A*. (*C*) Example diffraction patterns from a single location before and after engine operation show that peaks have returned to nearly identical positions.

thermocouple data were continuously collected with high temporal resolution. Stroboscopic data slicing and synchronization of the neutron data and sample logs were carried out using the VDRIVE software (21), which allowed for the creation of ensemble diffraction patterns in 20-s time bins. This combination of cyclic repetitions (21 cycles) and time bin size (20 s) was based on estimates from the previous static measurements of the accumulated beam time required to achieve a usable statistical ensemble within a given time bin. In general, achieving a smaller time bin size will require a proportionally larger number of repetitions. The binned ensemble diffraction data are shown in Fig. 7*A*; the shifts of both FCC(311) and FCC(222) peaks are primarily the result of thermal expansion of the alloy induced by the thermal cycling of the engine, and this figure demonstrates the feasibility of the stroboscopic approach.

Whereas single-peak fitting of d_{311} was used in the spatial mapping at static or steady-state conditions shown in Figs. 5 and 6, the size of the statistical ensemble is considerably smaller for each diffraction pattern in the time-resolved measurements, making that approach less practical. In order to obtain the time-resolved lattice parameter variation with the lowest statistical fitting error, full pattern Rietveld refinement was employed, which uses a least squares regression approach to fit a multiparameter line profile to the entire measured diffraction spectra rather than individual peaks (27) as shown in Fig. 7*B*. This was implemented on each of the sliced diffraction patterns using General Structure Analysis System (28) and EXPGUI software (29), and the lattice parameters of the Al alloys were extracted as $a(t, y, z)$ for each location. The time-resolved lattice strain was then calculated in an analogous way to Eq. **2**, where the lattice parameter a was used in place of d_{311}:

$$\epsilon(t, y, z) = \frac{a(t, y, z) - a^0(y, z)}{a^0(y, z)}. \qquad [3]$$

The time-resolved ensemble lattice strain at the two locations are plotted in Fig. 8 along with representative single-cycle measurements of exhaust gas temperature and IR surface temperature measured on the cylinder head. When the engine was started at idle, the temperature rose rapidly at first and asymptotically approached a steady condition. A similar pattern of temperature rise and asymptotic approach was seen when the generator load was increased to 2 kW. When the engine was turned off at 7 min, the exhaust gas temperature dropped quickly because the thermocouple was located in the core, or hottest part, of the gas flow, which ceased immediately upon shutdown. Conversely, the IR surface temperature showed a brief but immediate increase because turning off the engine also turned off the cooling fan mounted on the generator. This caused the surface convective heat transfer to decrease, and the continuing conductive heat transfer from the hotter interior of the cylinder head caused the surface temperature to increase temporarily before reversing trend and decreasing at a considerably slower rate than the exhaust temperature. The ensemble strain data are plotted in 20-s

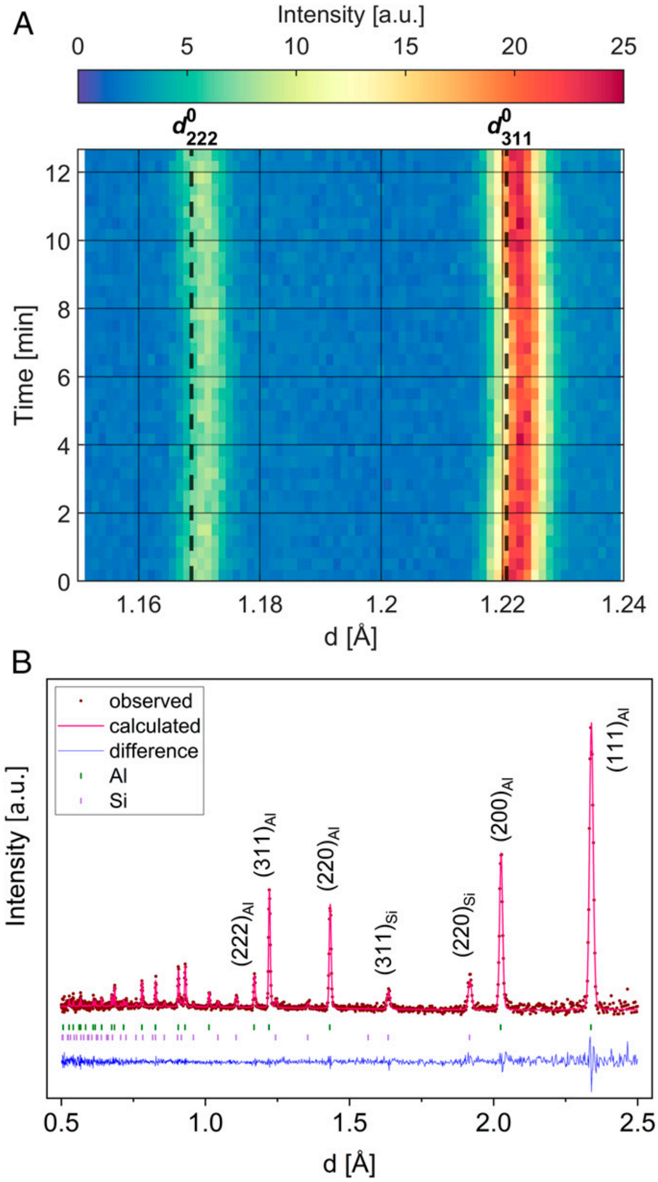

Fig. 7. (*A*) The cylinder head lattice Al (222) and Al (311) evolutions during the engine load cycle. Data are shown as 20-s time bins summed over an ensemble of 21 load cycles, with lattice shifts relative to the room temperature values corresponding to the temperature variation inside the engine during the load cycle. Reference values d^0_{222} and d^0_{311} were calculated from the measured $a^0 = 4.0485(3)$ Å using Eq. **1**. (*B*) Typical TOF diffraction pattern from the engine block with Rietveld refinement. Both the Al phase and the Si-containing intermetallic phase are observed and fit.

time bins as described above, and the lattice strain curves at both locations are very similar to the temperature curves with three distinct phases corresponding to the changes in engine load. The measurement location in the cylinder block had a lower strain, indicating lower temperature than the point in the cylinder head, and is in agreement with the IR images in Fig. 8 and the steady-state strain mapping shown in Fig. 5*D*.

The lattice strain measured inside the cylinder head is plotted against the IR temperature measured on the surface of cylinder head in Fig. 9. A few caveats should be noted regarding this comparison: the lattice strain may be induced by mechanical loading in addition to thermal expansion; the gauge volume measured by neutron diffraction is below the surface by an unknown distance on the order of the gauge length (5 mm), whereas the IR camera measures emission from the surface; the emissivity for the IR measurement was calibrated by a surface thermocouple at a single point on the cylinder head and is assumed the be uniform for the entire cylinder head; the IR measurement is taken from a single load transient cycle out of a series of cycles that were performed offline (not simultaneous with the neutron diffraction measurement) and was extracted from the IR movie by averaging over a 3 × 3 pixel region that was manually selected as being the closest surface location to the neutron gauge volume as seen by the sample positioning camera; and the cylinder head has a complex geometry of cooling fins which gives rise to considerable local variation in surface temperature. With those qualifications established, Fig. 9 does show a strong correlation between the surface temperature and the subsurface lattice strain ($R^2 = 0.95$). The data were fitted using a linear least squares regression, with the scaled error associated with each point used to weight the data as $\omega_i = (\max(\sigma_x)/\sigma_{x,i})^2 + (\max(\sigma_y)/\sigma_{y,i})^2$ in addition to the use of bisquare weights in the residual minimization to reduce the impact of outliers. The resulting slope of $(25.78 \pm 2.01) \times 10^{-6}$ $°C^{-1}$ is roughly 10% larger than the reported CTE of the material but is in very reasonable agreement given the caveats noted above and indicates that the lattice strain is caused predominantly by thermal expansion. The strong correlation between the neutron diffraction data and the other measures of dynamic system behavior seen in Figs. 8 and 9 demonstrates that stroboscopic neutron diffraction is capable of nondestructively probing the dynamic lattice strain evolution during transient operation in a running engine.

Challenges and Limitations. In contrast to the well-characterized and intentionally designed samples that are typically used for neutron studies, in situ investigations of real engineering devices and systems present several challenges.

Geometric complexity. Real devices often have complex geometric features such as the cooling fins on the engine studied here. Even if the nominal geometry is known a priori, which is not always the case, variabilities arising from casting or other fabrication processes may introduce uncertainty regarding the actual dimensions of the sample. This can create difficulties in sample alignment and placement of the gauge volume. The use of fiducial markers with a laser scanning and alignment system is important for repeatably locating the sample in space but will generally not provide information about internal features of the sample.

Vibration and motion. Extracting meaningful results from the diffraction data requires some information about what part of the material is generating the scattering signal being measured. In the case of a static sample, this is straightforward as the same material is always present within the gauge volume. In the case of a vibrating sample with random or asynchronous oscillations relative to the neutron pulse, the size of the gauge volume is effectively increased but with an uneven sampling of the volume. Therefore, it is generally advisable to maintain the displacement of the gauge volume below 10% of the gauge length. A similar challenge is presented by translating or rotating components, although this can be overcome if the motion can be synchronized with the neutron pulse or if the position can be measured in real time to allow for data reduction in post processing.

Grain sizes. Grain size and orientation can be important factors in the practice of using diffraction to measure lattice strain in bulk materials. If a single grain occupies a substantial portion of the gauge volume, the scattering response becomes anisotropic, producing spotty diffraction patterns and misleading results. This was not an issue in the present work, as the grain size of the AlCe alloy (10 to 100 μm) (20) was small relative to the gauge volume ($5 \times 5 \times 5$ mm^3). This highlights a strength of neutrons relative to other techniques such as synchrotron X-rays, which typically use much smaller gauge volumes.

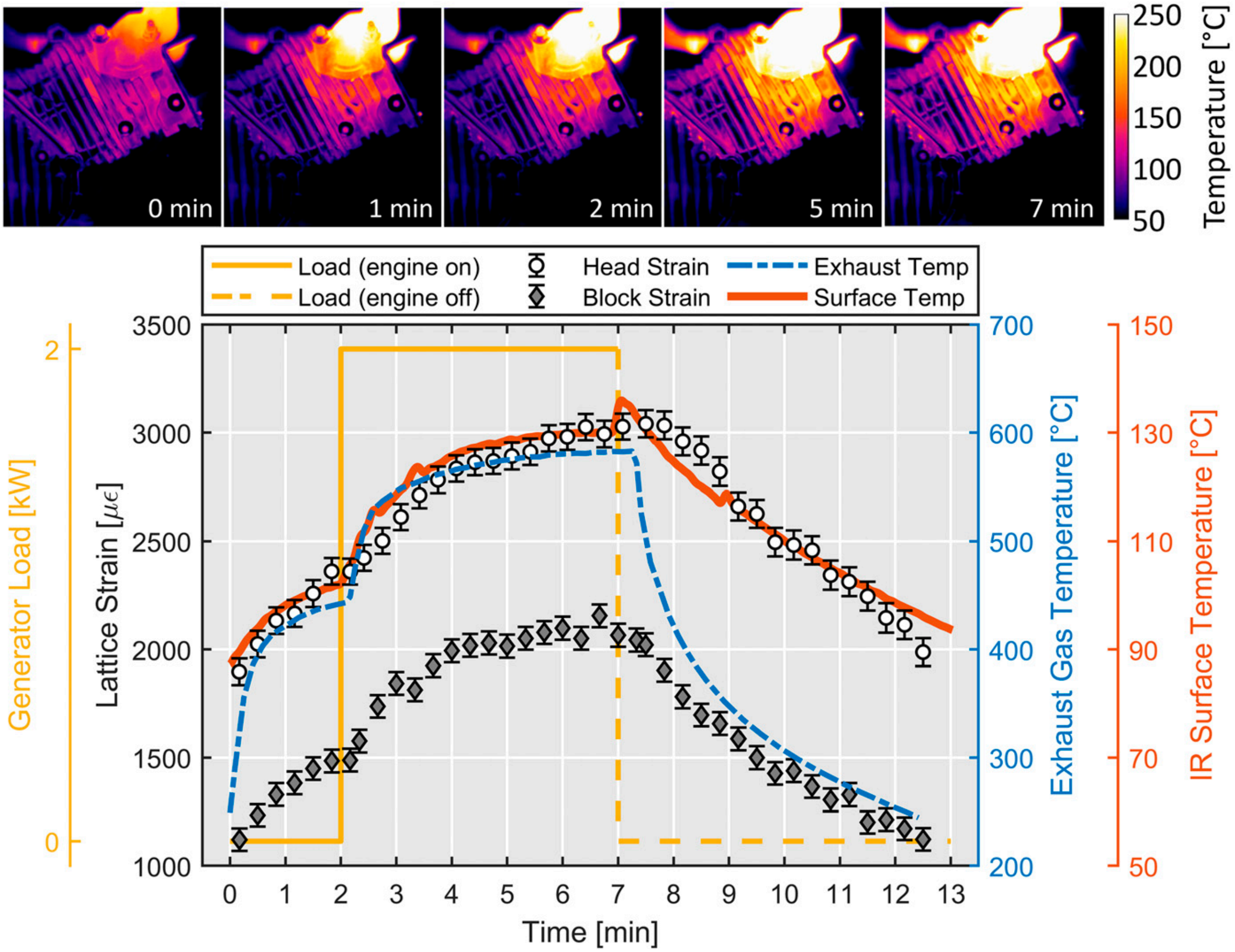

Fig. 8. (*Top*) Sequence of IR images showing evolution of surface temperature during a load transient cycle. (*Bottom*) Ensemble lattice strain response from selected locations measured within cylinder block and cylinder head by neutron diffraction during load transient cycles compared with single-cycle measurements of exhaust gas temperature and cylinder head IR surface temperature.

Attenuation and scattering. Large samples can present challenges due to attenuation of both the incident and diffracted neutrons, with each material having macroscopic attenuation coefficients due to absorption, coherent scattering, and incoherent scattering. While Al is highly transparent with a combined 1/e penetration depth of 102 mm (1 Å neutrons), Fe causes significantly higher attenuation with a 1/e penetration depth of 9 mm. The large incoherent scattering cross section of ^{1}H means that hydrogenous materials such as plastic, coolant, lubricant, and fuel may present more serious challenges, with a 1/e penetration depth of only 1.8 mm for water (30). Attenuation of the incident beam reduces the rate at which neutrons reach the gauge volume, increasing the amount of time required to make statistically meaningful measurements. The same is true for the neutrons scattered from the gauge volume toward the detector, with the additional complication that heterogenous composition or geometry of the material between the gauge volume and the detector can cause shadowing on the detector. Highly scattering materials may also increase the background count rate, further increasing the required counting time. Generally recommended approaches are to remove or replace the solid components such as steel, plastic, or other attenuating materials with Al where possible. In high-temperature systems where the strength of Al is a limitation, Ti may also be used. Similarly, hydrogenous liquids may be replaced by fluorinated equivalents where possible. In instances where substitution of attenuating components is not desirable or practical, special sample orientations may also be used to avoid interferences.

Activation. While neutron diagnostics are generally nondestructive from the perspective of mechanical or chemical alteration of samples, neutron-induced radioactivity (activation) does pose a concern for certain materials. Activation is a function of the isotopic composition and quantity of the material as well as the neutron flux and cumulative exposure time. As an example, natural Al is composed entirely of the stable isotope ^{27}Al, which has a small neutron absorption cross section of 1.495 barn. Its activation product ^{28}Al has a relatively short half-life of 2.245 m, which means that even highly activated samples may decay below releasable radioactivity limits in a matter of hours or days. In contrast, many steel alloys contain Co in concentrations ranging from trace amounts up to 8% in M42 high-speed tool steel. The only stable isotope, ^{59}Co, has a relatively large neutron absorption cross section of 37.18 barn, and its activation product, ^{60}Co, has a half-life of 5.275 y (30). Depending on the Co concentration and total neutron exposure, steel samples may require days or decades to decay below releasable radioactivity limits. It is

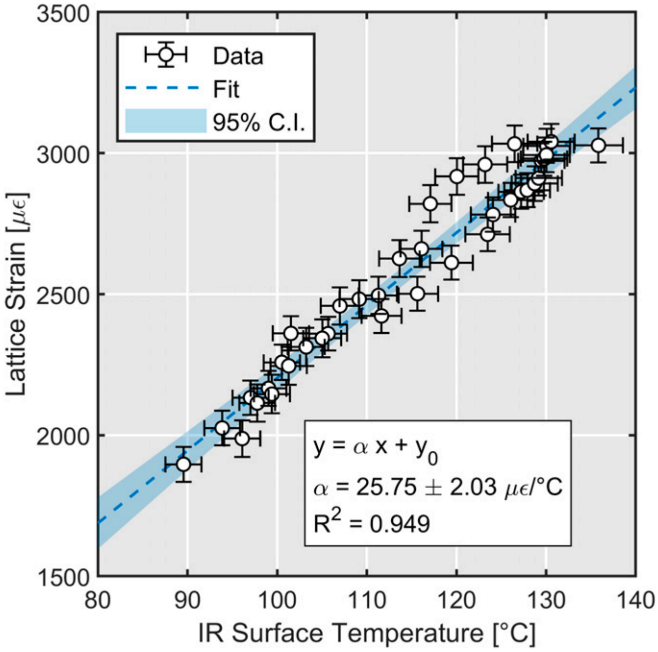

Fig. 9. Lattice strain measured below the surface of the cylinder head by neutron diffraction shows strong correlation to temperature measured on the surface of the head by infrared camera.

therefore important that users have as much information as possible regarding the composition of their samples beforehand, and users should always be prepared for the possibility that samples may not be immediately releasable.

Summary and Outlook

We have demonstrated the operando lattice strain measurement of ICE components by neutron diffraction. Spatial variation in lattice strains induced by thermal gradients in the cylinder block and cylinder head were mapped at a steady state loaded condition, and the trends agreed with external infrared surface temperature measurements. The time-resolved dynamic response of the lattice strain during engine load cycling was resolved at two locations in 20-s time bins by the asynchronous stroboscopic neutron diffraction approach, demonstrating that the operando neutron measurement can allow for understanding of in-service materials behaviors in complex engineering devices. The dynamic response in lattice strain mirrored that of the temperature measurements, and the lattice strain measured in the cylinder head was strongly correlated to the infrared temperature measurement on the surface of the cylinder head.

The development of this technique for measurement of operational strains experienced by ICEs will enable the study of complex load states and thermal gradients throughout the volume of the solid components. Spatially and temporally resolved understanding of these systems has previously been accessible only via models supported by point measurements such as fast-response thermocouples. The ability to provide experimental validation and boundary condition data at similar scales and spatial extent to the domains explored in next-generation exascale models will broaden the impact of engineering neutron diffraction by increasing the user base while also increasing our knowledge of material behavior under complex and extreme operating conditions.

This study also serves as a baseline for the development of a dedicated neutron diffraction research engine which is ongoing at ORNL. Whereas the small air-cooled engine used in this study was chosen principally for its ease of implementation and was manually operated to achieve 20-s temporal resolution, the platform under development will be representative of modern automotive engines and will feature tight integration between the engine controller and the neutron diffractometer data acquisition system to achieve subms temporal resolution in stroboscopic operation. This engine will also serve as a modular research platform to enable access to other users who may wish to investigate the performance of novel materials under true engine operating conditions. The approach adopted in this study for the rapid prototyping of molds to produce a cylinder head from an AlCe alloy and perform operando lattice strain measurements in that component while being used in a real engine serves as an example of how users may leverage the manufacturing, transportation, and neutron user facilities at ORNL to investigate the in-service behavior of materials without having to design the entire experimental apparatus from the ground up.

Data Availability. Lattice strain and other supporting data are available at https://doi.org/10.13139/ORNLNCCS/1728670.

ACKNOWLEDGMENTS. This work was supported by the US Department of Energy (DOE), Office of Energy Efficiency and Renewable Energy, Vehicle Technologies Office, via the Advanced Combustion Engine Systems program. This research used resources at the SNS, a DOE Office of Science User Facility, and the NTRC, a DOE Office of Energy Efficiency and Renewable Energy User Facility, both operated by ORNL. The research on AlCe alloys was sponsored by the Critical Materials Institute, an Energy Innovation Hub funded by the DOE, Office of Energy Efficiency and Renewable Energy, Advanced Manufacturing Office and Eck Industries. This work was performed under the auspices of the DOE with ORNL under contract DE-AC05-00OR22725. We acknowledge the contributions of Steven Whitted at ORNL, who performed the modification and packaging of the engine for operation in the diffractometer. This manuscript has been authored by UT-Battelle, LLC, under Contract DE-AC05-00OR22725 with the US DOE. The US Government retains and the publisher, by accepting the article for publication, acknowledges that the US Government retains a nonexclusive, paid-up, irrevocable, worldwide license to publish or reproduce the published form of this manuscript, or allow others to do so, for US Government purposes. The DOE will provide public access to these results of federally sponsored research in accordance with the DOE Public Access Plan (energy.gov/downloads/doe-public-access-plan). Support for DOI 10.13139/ORNLNCCS/1728670 dataset is provided by the US Department of Energy, project IPTS-18431 under Contract DE-AC05-00OR22725. Project IPTS-18431 used resources of the Oak Ridge Leadership Computing Facility at Oak Ridge National Laboratory, which is supported by the Office of Science of the US Department of Energy under Contract No. DE-AC05-00OR22725.

1. J. B. Heywood, *Internal Combustion Engine Fundamentals* (McGraw-Hill Education, ed. 2, 2018).
2. H. Mahle Gmb, *Pistons and Engine Testing* (Vieweg+Teubner Verlag, ed. 1, 2013).
3. Z. Wang *et al.*, Analysis of pre-ignition to super-knock: Hotspot-induced deflagration to detonation. *Fuel* **144**, 222–227 (2015).
4. C. Rakopoulos, G. Kosmadakis, E. Pariotis, Critical evaluation of current heat transfer models used in CFD in-cylinder engine simulations and establishment of a comprehensive wall-function formulation. *Appl. Energy* **87**, 1612–1630 (2010).
5. L. M. Pickett, J. J. Lopez, "Jet-wall interaction effects on diesel combustion and soot formation" (SAE Technical Paper 2005-01-0921, 2005). https://doi.org/10.4271/2005-01-0921.
6. W. Wu *et al.*, PIND: High spatial resolution by pinhole neutron diffraction. *Appl. Phys. Lett.* **112**, 253501 (2018).
7. K. An *et al.*, RHEGAL: Resistive heating gas enclosure loadframe for *in situ* neutron scattering. *Rev. Sci. Instrum.* **89**, 092901 (2018).
8. G. E. Granroth *et al.*, Event-based processing of neutron scattering data at the Spallation Neutron Source. *J. Appl. Cryst.* **51**, 616–629 (2018).
9. W. Wu *et al.*, Bending behavior of a wrought magnesium alloy investigated by the in situ pinhole neutron diffraction method. *Crystals* **8**, 348 (2018).
10. D. Yu *et al.*, Tracing phase transformation and lattice evolution in a TRIP sheet steel under high-temperature annealing by real-time in situ neutron diffraction. *Crystals* **8**, 360 (2018).
11. D. Yu *et al.*, Real-time in situ neutron diffraction investigation of phase-specific load sharing in a cold-rolled TRIP sheet steel. *JOM* **70**, 1576–1586 (2018).
12. M. T. Hutchings *et al.*, *Introduction to the Characterization of Residual Stress by Neutron Diffraction* (CRC Press, 2005).

13. K. An *et al*., First in situ lattice strains measurements under load at VULCAN. *Metall. Mater. Trans. A* **42**, 95–99 (2011).
14. K. An, Y. Chen, A. D. Stoica, VULCAN: A “hammer” for high-temperature materials research. *MRS Bull.* **44**, 878–883 (2019).
15. R. Riedel, “Overview of data acquisition at the SNS.” NOBUGS 2004 Conference, October 18-20, 2004, Paul Scherrer Institute, Switzerland (Oak Ridge National Laboratory Internal Report, 2004). http://lns00.psi.ch/nobugs2004/papers/paper00055.pdf.
16. K. An *et al*., *Asynchronous In Situ Neutron Scattering Measurement of 10 μs Transient Phenomena at Spallation Neutron Source* (Oak Ridge National Laboratory, Oak Ridge, TN, 2012).
17. Z. Z. Yu *et al*., “In-situ neutron diffraction study of non-equilibrium phase transformation in advanced high-strength steels” in *Trends in Welding Research: Proceedings of the 9th International Conference, S. Babu, H. K. Bhadeshia, C. E. Cross, S. A. David, T. DebRoy, J. DuPont, T. Koseki, S. Liu, Eds.* (ASM International, 2013), pp. 506–509.
18. Z. Z. Yu *et al*., “Measurement of steel Phase Transformation Kinetics by Dilatometry and In-Situ Neutron Diffraction–A Comparative Study” in *Trends in Welding Research: Proceedings of the 9th International Conference, S. Babu, H. K. Bhadeshia, C. E. Cross, S. A. David, T. DebRoy, J. DuPont, T. Koseki, S. Liu, Eds.* (ASM International, 2013), pp. 510–513.
19. H. B. Henderson *et al*., Additively manufactured single-use molds and reusable patterns for large automotive and hydroelectric components. *Int. J. MetalCast.* **14**, 356–364 (2020).
20. Z. C. Sims *et al*., High performance aluminum-cerium alloys for high-temperature applications. *Mater. Horiz.* **4**, 1070–1078 (2017).
21. K. An, *VDRIVE—Data Reduction and Interactive Visualization Software for Event Mode Neutron Diffraction, ORNL TM-2012-621* (Oak Ridge National Laboratory, 2012).
22. N. Fuhrmann *et al*., Two-dimensional cycle-resolved exhaust valve temperature measurements in an optically accessible internal combustion engine using thermographic phosphors. *Appl. Phys. B* **106**, 945–951 (2012).
23. F. Köpple *et al*., Experimental investigation of fuel impingement and spray-cooling on the piston of a GDI engine via instantaneous surface temperature measurements. *SAE Int. J. Eng.* **7**, 1178–1194 (2014).
24. F. Schulz *et al*., Gasoline wall films and spray/wall interaction analyzed by infrared thermography. *SAE Int. J. Eng.* **7**, 1165–1177 (2014).
25. N. Dolatabadi *et al*., Influence of advanced cylinder coatings on vehicular fuel economy and emissions in piston compression ring conjunction. *Appl. Energy* **259**, 114129 (2020).
26. ASM International Handbook Committee, “Properties of cast aluminum alloys” in *ASM Handbook, Volume 02 - Properties and selection: nonferrous alloys and special-purpose materials* (ASM International, 1990), pp. 152–177.
27. H. Rietveld, A profile refinement method for nuclear and magnetic structures. *J. Appl. Cryst.* **2**, 65–71 (1969).
28. A. C. Larson, R. B. Von Dreele, General Structure Analysis System (GSAS), Los Alamos National Laboratory Report LAUR 86-748 (2004).
29. B. H. Toby, EXPGUI, a graphical user interface for GSAS. *J. Appl. Cryst.* **34**, 210–213 (2001).
30. P. Kienzle, Neutron activation and scattering calculator. NIST Center for Neutron Research. https://www.ncnr.nist.gov/resources/activation/. Accessed 1 December 2020.